Inorganic Chemistry

Article

pubs.acs.org/IC

X-ray Magnetic Circular Dichroism Investigation of the Electron Transfer Phenomena Responsible for Magnetic Switching in a Cyanide-Bridged [CoFe] Chain

Michael L. Baker,[‡] Yasutaka Kitagawa,[†] Tetsuya Nakamura,[§] Kou Tazoe,[‡] Yasuo Narumi,[‡] Yoshinori Kotani,[§] Fumichika Iijima,[∥] Graham N. Newton,[∥] Mitsutaka Okumura,[†] Hiroki Oshio,[∥] and Hiroyuki Nojiri*[,‡]

[‡]Institute for Materials Research, Tohoku University, Sendai 980-8577, Japan

[†]Graduate School of Science, Osaka University, Toyonaka, Osaka 560-0043, Japan

[§]Japan Synchrotron Radiation Research Institute/SPring-8, Sayo, Hyogo 679-5198, Japan

[∥]Graduate School of Pure and Applied Sciences, Department of Chemistry, University of Tsukuba, Tennodai 1-1-1, Tsukuba 305-8571, Japan

Supporting Information

ABSTRACT: The cyanide-bridged [CoFe] one-dimensional chain, $[Co^{II}((R)\text{-pabn})][Fe^{III}(Tp)(CN)_3](BF_4)\cdot MeOH\cdot 2H_2O$, where (*R*)-pabn = (*R*)-*N*2,*N*(2′)-bis(pyridin-2-ylmethyl)-1,1′-binaphthyl-2,2′-diamine and Tp = hydrotris(pyrazolyl)borate, exhibits magnetic and electric bistabilities originating from an electron transfer coupled spin transition between Fe−CN−Co pairs. The use of L-edge X-ray absorption spectroscopy (XAS) in combination with L-edge X-ray magnetic circular dichroism (XMCD) is explored for the investigation of the electronic structure and magnetization of Co and Fe ions separately, in both diamagnetic and paramagnetic states. It has been established from susceptibility results that the switching between diamagnetic and paramagnetic phases emanates from electron transfer between low spin Fe(II) and Co(III), resulting in low spin Fe(III) (*S* = 1/2) and high spin Co(II) (*S* = 3/2). The XAS and XMCD results are consistent with the bulk susceptibility measurements, where greater detail regarding the charge transfer process is determined. The Fe−CN−Co electron transfer pathway is highlighted by a strongly XMCD dependent transition to a cyanide back bonding orbital, giving evidence for strong hybridization with Fe(III) t_{2g} orbitals. In addition to thermally induced and photoinduced switching, [CoFe] is found to exhibit a switching by grinding induced dehydration. Analysis of XAS shows that on grinding diamagnetic [CoFe], 75% of metal ions lock into the magnetic Co(II)Fe(III) phase. Density functional theory calculations based on the [CoFe] crystal structure in the magnetic and nonmagnetic phases aid the spectroscopic results and provide a complementary insight into the electronic configuration of the [CoFe] 3d shells, quantifying the change in ligand field around Co and Fe centers on charge transfer.

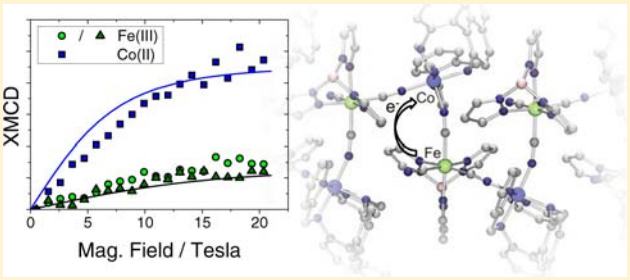

INTRODUCTION

The manipulation of metal-to-metal charge transfer (MMCT) within magnetic complexes inspires the design of new multifunctional magnetic systems.[1] In such compounds, sensitivity to changes in redox potential between ion pairs is exploited for the control of electronic properties. MMCT and its accompanying switching of magnetic and electronic properties can be controlled by external stimuli such as photoillumination, heat, and pressure.[2] The study of Prussian blue analogues, a class of cyanide-bridged polynuclear materials, has shown considerable success in the pursuit of switchable magnetic phenomena.[3] Recent work has focused on discrete analogues[4] of heterometallic cyanide bridged complexes and has led to the emergence of one-dimensional systems.[5] The synthesis of one-dimensional MMCT systems exhibiting single chain magnet properties[6] in conjunction with switchable magnetism is the focus of much research in the search for advanced functionality within magnetic compounds.

Here we investigate a one-dimensional square wave shaped cobalt−cyanide−iron chain, $[Co^{II}((R)\text{-pabn})][Fe^{III}(Tp)(CN)_3](BF_4)\cdot MeOH\cdot 2H_2O$, abbreviated [CoFe] (see Figure 1), where (*R*)-pabn = (*R*)-*N*2,*N*(2′)-bis(pyridin-2-ylmethyl)-1,1′-binaphthyl-2,2′-diamine and Tp = hydrotris(pyrazolyl)-borate. The structure exhibits chirality originating from the (*R*)-pabn ligand. The system has received much attention for its multifunctional magnetic and electronic properties, which include the exhibition of single chain magnetism, diamagnetism,

Received: June 25, 2013
Published: December 4, 2013

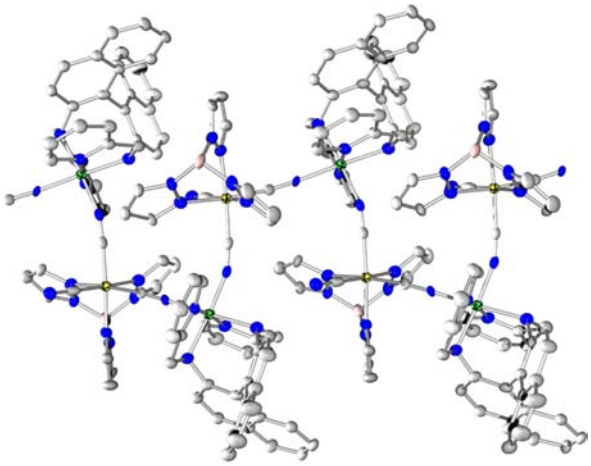

Figure 1. The structure of [CoFe]. The yellow spheres are Fe, the green spheres are Co, the gray spheres are C, the blue spheres are N, and the pink spheres are B.

and paramagnetism, and its interchangeability between insulating and semiconducting states, where reversible MMCT switching between phenomena is induced by photoillumination or heat.[7]

The characterization of magnetic response to external stimuli within discrete MMCT systems is typically performed in the bulk via magnetometry, while X-ray structural analysis and Mössbauer spectroscopy provide some insight at an atomic level. Such measurements on [CoFe] confirm that MMCT induces a spin crossover from a diamagnetic phase (DP), Co(III)Fe(II) (both $t_{2g}^6e_g^0$), to a paramagnetic phase (MP), Co(II)Fe(III) ($t_{2g}^5e_g^2$ and $t_{2g}^5e_g^0$, respectively).[7] The MMCT process, from the DP to the MP, occurs at a critical temperature of ∼314 K; this is clearly detected in the temperature dependence of the magnetic susceptibility, observed as a broad thermal hysteresis. Photon irradiation induced MMCT below 5 K results in a rapid increase in magnetization. AC susceptibility measurements of the photon irradiation induced excited state show in and out of phase signals composed of a major and a minor relaxation process. The major species corresponds to single chain magnetism, and the minor species corresponds to a degree of chain fragmentation. Furthermore, DC conductivity confirms that thermally induced MMCT (DP to MP) coincides with an increase in conductivity, from insulating to semiconducting.

In this investigation, we use L-edge X-ray absorption spectroscopy (XAS) and X-ray magnetic circular dichroism (XMCD) in conjunction with density functional theory (DFT) calculations to characterize MMCT within [CoFe]. L-edge XAS probes from 2p to 3d orbitals and is electrodipole allowed, meaning that the L-edge XAS intensity is directly proportional to the d-character of the 3d unoccupied orbitals.[8] Hence, XAS contains detailed information regarding the nature of MMCT configurations at a molecular orbital level. For these reasons, XAS has been used quite extensively in the characterization of charge transfer, including fundamental investigations of π and σ orbital bonding and back-bonding,[9] in the study of several Prussian blue analogue systems[10−12] and the investigation of biological functions within iron porphyrins.[13] Such studies have been performed in zero applied magnetic field and have relied on ligand field multiplet simulations, based on effective models with simplified atomic symmetries, to interpret spectra and obtain parameters such as $10Dq$ terms and electron transfer potential energies. In this investigation, the advantages of measuring XMCD in the study of MMCT is explored. The XMCD signal is inherently weak relative to XAS; however with the development of lower temperature sample environments and higher applied magnetic fields, the use of L-edge XMCD for the study of paramagnetic and molecular based transition metal systems has shown a vibrant increase in recent years.[14] The potential of XMCD has been demonstrated for the characterization of magnetic properties in molecule based magnets, in the bulk,[15] and on surfaces.[14,16] In this study, XMCD measurements are used to provide an atomic specific measurement of magnetization, highlighting the presence of unpaired electrons within the 3d orbitals and their hybridization with ligand orbitals. Because these XMCD signals increase with applied magnetic field, we measure XMCD to high magnetic fields up to 21 T. Furthermore, DFT calculations are employed, based on the DP and MP crystal structures, to aid the analysis of our spectroscopic findings.

The discovery of a new physical process within [CoFe] is reported, an irreversible MMCT induced by the release of coordinated water molecules upon grinding of a sample of [CoFe] (temporarily applied, with a pestle and mortar). It is found that this process locks the system into the magnetic phase. Grinding assisted MMCT to our knowledge has not been previously reported. The grinding assisted MMCT differs from the pressure activated switching observed on other MMCT systems because the sample remains completely locked in the magnetic state after the application of pressure is elevated. This control over the magnetic phase of [CoFe] provides a very convenient way to allow for a detailed investigation into the valence phases present in [CoFe] using Soft XAS and XMCD.

EXPERIMENTAL SECTION

XAS and XMCD Measurements. XAS and XMCD spectra were measured on the BL25SU beamline at SPring-8 synchrotron user facility, Hyogo, Japan. XAS spectra in the energy region of both Co and Fe L-edges were measured with an applied constant magnetic field of 1.9 T at 15.3 K. The monochromation of incident circularly polarized X-rays was performed using a varied line-spacing plane grating with 600 lines/mm. Radiation damage due to X-ray overexposure is limited by use of a shutter system reducing exposure for each incident X-ray energy to 200 ms. In addition to electromagnet measurements, recent development at the beamline has seen the integration of a pulsed magnetic field system for soft XMCD measurements.[17] For incident X-ray energies exhibiting strong XMCD, the magnetic field dependence was measured up to 21 T. Incident X-rays are synchronized with the applied field pulse within the shutter opening period. The measurements of positively (negatively) circularly polarized incident X-rays are applied parallel (antiparallel) to the applied field direction (μ^+ and μ^- respectively). Pulsed magnetic fields were generated with a compact capacitor bank delivering a total energy of 37 kJ at a charge voltage of 1.7 kV. The examined polycrystalline samples of [CoFe] were mixed with gold (20%) to improve conductivity for the measurement of the XAS signal by total electron yield. The diamagnetic phase samples were prepared carefully, without application of pressure on mixing with gold. Preparation of the MP CoFe by grinding induced MMCT was performed at room temperature using a pestle and mortar. Evidence of the MMCT switching process is immediately apparent as the application of grinding results in a color change of the sample from a dark green to dark red. The equivalent change in color is observed when the sample is heated over 320 K.

Computational Details. The structures for the DFT calculations are based on the coordinates of the [CoFe] unit determined by X-ray

dx.doi.org/10.1021/ic402580n | Inorg. Chem. 2013, 52, 13956−13962

crystallography. The Fe−Co heterodimer unit is illustrated in Figure 2. The DP and MP are obtained from the 100 and 295 K crystal

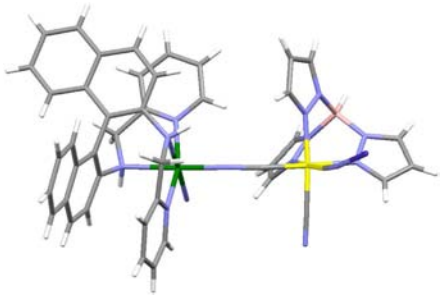

Figure 2. The [CoFe] 295 K structural unit on which DFT calculations are based.

structures, respectively. For the high temperature Fe(III)Co(II) phase, ferromagnetic (FM) and antiferromagnetic (AFM) spin coupling states are calculated to estimate the magnetic coupling value (J). Calculations for the MP show that the energy difference between the FM and AF states is close to the energy resolution of the XAS measurement (fwhm 0.1 eV). Hence, despite both states being populated during the experimental measurements, for simplicity discussion is focused on the FM results. Further details regarding the DFT results for DP and MP (AF and FM) calculations can be found in the Supporting Information section.

The electronic structures of the structure models and charge-spin states are calculated by the use of a hybrid DFT of the Becke-3 Lee−Yang−Parr (B3LYP) functional set on Gaussian 09. The basis functions used for all calculations are Huzinaga MIDI plus p-type orbitals for Fe and Co ions, 6-31+G* for cyanide ligands, and 6-31G* for other atoms. For the diamagnetic state that consists of the low spin Fe(II) and Co(III) ions, a spin-restricted calculation is applied. For the open-shell (FM and AF) states, which consist of Fe(III) and Co(II) ions, a broken-symmetry (BS) calculation is employed to approximate the static correlation by the quasi-degenerate orbitals and to express localized spins on each metal site.

RESULTS AND DISCUSSION

XAS and XMCD. The diamagnetic and magnetic phase of [CoFe] are investigated at both the Fe and Co L-edges. The general spectral shape of the L-edge XAS has contributions separated in energy due to spin orbit coupling within the 2p state. The spin orbit coupling nondegeneracy is of approximately 15−20 eV, corresponding to the splitting between the J = 3/2 (L_3-edge) and the J = 1/2 (L_2-edge). The technique is an element and valence specific probe of ligand field symmetry and valence shell composition. Additionally, XAS is sensitive to orbital covalence, providing insight into metal to ligand charge transfer (MLCT) and ligand to metal charge transfer (LMCT). The presence of charge transfer is observed in the form of additional XAS transitions, causing changes to the L-edge spectral shape, including the addition of satellite features to the L_3 and L_2 edges. In the ground state, the metal d^N configuration hybridizes with the possible MLCT ($d^{N-1}L^-$) and the LMCT ($d^{N+1}L^+$) configurations. The carbon and nitrogen atoms comprising the cyanide ion bridge between Fe and Co act as strong σ donors and π acceptors. With such sensitivity to bonding, structure, and valence composition, XAS is used to identify and characterize the MMCT and the resultant valence states of CoFe.

Fe L-edge. Polarized X-ray absorption spectra ($\mu^+ + \mu^-$) for the Fe L-edge (Figure 3a,b) show several aspects of the [CoFe] spectra are unchanged in both the DP and MP. At the Fe L_3-

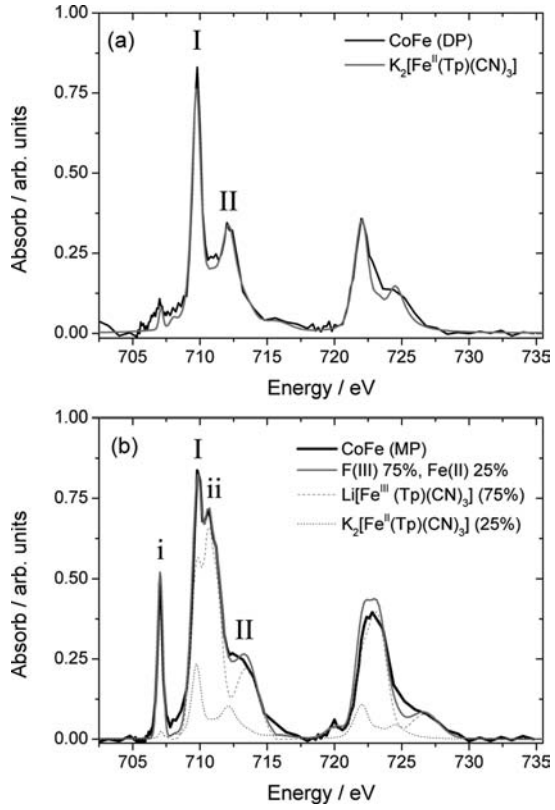

Figure 3. XAS energy spectra for the Fe L-edge of [CoFe] in the DP (a) and the MP (b) compared with the reference compounds $Li[Fe^{III}(Tp)(CN)_3]$ and $K_2[Fe^{II}(Tp)(CN)_3]$.

edge, these features include the main absorption at 709.8 eV (I) and the broad absorption at 712.2 eV (II) (observed as a shoulder in the MP). However, additional features are apparent in the MP, marked in Figure 3 as i and ii. Several of the observed Fe XAS features are common to known cyanide coordinated octahedral Fe moieties. Transition i is the fingerprint for low spin Fe(III), observed only in the MP as a consequence of the addition of a hole in the t_{2g}^5 symmetry orbitals with respect to closed shell t_{2g}^6. For example, similar Fe L-edge XAS have been previously observed in the study of $K_3[Fe^{III}(CN)_6]$ and $K_4[Fe^{II}(CN)_6]$ monomer complexes[9,13] and Prussian blue analogue systems.[11,12,18] Comparison with these systems draws a tentative identification of the major features observed in the Fe L-edge of [CoFe]. The origin of I is identified as resulting predominantly from the $|2p^6t_{2g}^6e_g^0\rangle \rightarrow |2p^5t_{2g}^6e_g^1\rangle$ and $|2p^6t_{2g}^5e_g^0\rangle \rightarrow |2p^5t_{2g}^5e_g^1\rangle$ transitions for Fe(II) and Fe(III) respectively. The higher energy satellite feature, II, is due to metal to ligand charge transfer, which mixes metal Fe d character into unoccupied cyanide ligand π^* orbitals. The corresponding XAS transition can be expressed as $|2p^6t_{2g}^5L^-e_g^0\rangle \rightarrow |2p^5t_{2g}^5L^-e_g^1\rangle$ and $|2p^6t_{2g}^4L^-e_g^0\rangle \rightarrow |2p^5t_{2g}^4L^-e_g^1\rangle$ for Fe(II) and Fe(III), respectively, where L^- corresponds to the donation of a 3d orbital electron to a ligand π^* orbital.

A more precise analysis of the Fe L-edge spectral contributions is obtained by comparison to equivalently ligated single ion clusters, low spin Fe(III) and low spin Fe(II), $Li[Fe^{III}(Tp)(CN)_3]$ and $K_2[Fe^{II}(Tp)(CN)_3]$. The DP Fe L-edge spectrum (Figure 3a) is coincident with $K_2[Fe^{II}(Tp)(CN)_3]$ demonstrating that the DP corresponds to the pure Fe(II) state. The MP L-edge spectrum (Figure 3b) is reproduced following the superimposition of $Li[Fe^{III}(Tp)$-

dx.doi.org/10.1021/ic402580n | Inorg. Chem. 2013, 52, 13956−13962

$(CN)_3$] and $K_2[Fe^{II}(Tp)(CN)_3]$ L-edge spectral features in a 3:1 ratio, demonstrating that the grinding assisted charge transfer effect is not complete. The fitting of $Li[Fe^{III}(Tp)(CN)_3]$ and $K_2[Fe^{II}(Tp)(CN)_3]$ to reproduce the MP Fe L-edge spectrum reveals that the transitions labeled I and II are present within the pure Fe(LS-III); however, I is somewhat less intense when the DP impurity is discounted and II is shifted up in energy very slightly with respect to the main L_3-edge peak.

Further details regarding the electronic structure of [CoFe] are obtained via the analysis of the individual polarized μ^+ and μ^- Fe L-edge spectra. Figure 4 shows the individual μ^+ and μ^-

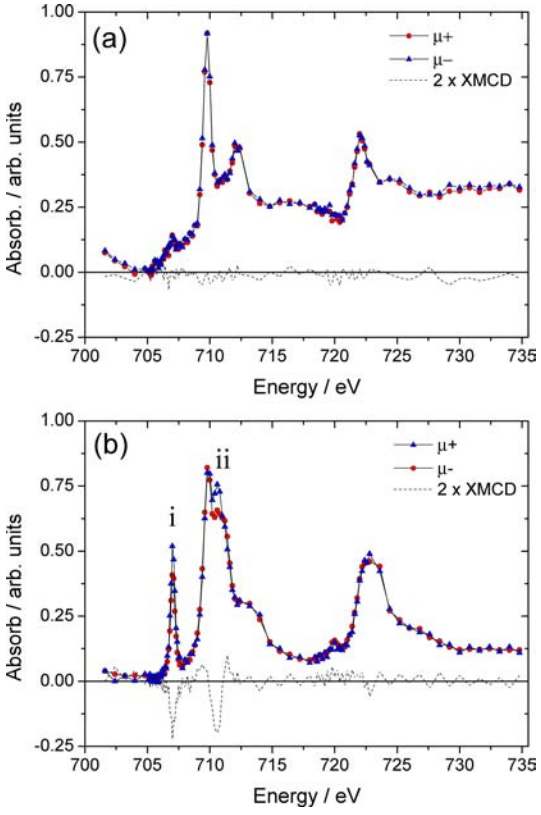

Figure 4. Circularly polarized XAS and XMCD energy spectra for the Fe L-edge of [CoFe] in the DP (a) and the MP (b) with an applied field of 1.9 T at 15 K.

polarized spectra, and their difference the XMCD, for the DP and the MP, measured with an applied external magnetic field of 1.9 T at 15 K. The DP spectrum shows dependence on the X-ray helicity in the limit given by the measurement background, as expected for the nonmagnetic phase. Only small deviations of the XMCD from zero are observed, which are not coincident with XAS intensities and are therefore not associated with paramagnetic transitions. Contrastingly XMCD is identified in the MP spectrum at the L_3-edge at the positions labeled i and ii.

The MP Fe(III) exhibits a low spin configuration and hence only one unpaired electron in the 3d shell. The XMCD intensity is hence expected at position i, relating to the half-filled 3d orbtial of the approximately t_{2g} symmetry set. It is striking to observe equivalent XMCD intensity at position ii. The XMCD intensity centered at ii highlights hybridization of the Fe(III) half-filled orbital with the surrounding cyanide ligand. Within this approximation, the magnetic dichroic dependence of the spectrum enables discrimination of state mixing via the t_{2g} symmetry between $|2p^6t_{2g}^5e_g^0\rangle \rightarrow |2p^5t_{2g}^6e_g^0\rangle$ and $|2p^6t_{2g}^4e_g^0L^-\rangle \rightarrow |2p^5t_{2g}^5e_g^0L^-\rangle$ transitions, identifying the charge transfer pathway. The near equivalent strength and magnetic field dependence of the XMCD signals exhibited in the Fe(III) L_3 (Figure 3) indicate considerable entanglement between the $|2p^5t_{2g}^6e_g^0\rangle$ and $|2p^5t_{2g}^5e_g^0L^-\rangle$ transition final states. It is confirmed, due to helicity independence, that transitions I and II for both DP and MP originate predominantly from transitions into e_g symmetry orbitals. For the DP, I and II correspond to the transitions $|2p^6t_{2g}^6e_g^0\rangle \rightarrow |2p^5t_{2g}^5e_g^1\rangle$ and $|2p^6t_{2g}^5e_g^0L^-\rangle \rightarrow |2p^5t_{2g}^5e_g^1L^-\rangle$. For the MP, I and II correspond to $|2p^6t_{2g}^5e_g^0\rangle \rightarrow |2p^5t_{2g}^5e_g^1\rangle$ and $|2p^6t_{2g}^4e_g^0L^-\rangle \rightarrow |2p^5t_{2g}^4e_g^1L^-\rangle$ respectively.

Co L-edge. The Co XAS of DP and MP [CoFe] exhibit coincidence in the energy of the primary L_3 and L_2 intensities with only subtle differences in line shape (Figure 5). The MP

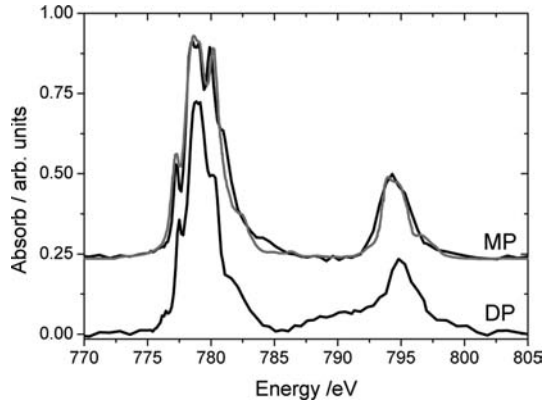

Figure 5. XAS energy spectra for the Co L-edge of [CoFe] in the DP and the MP measured at 15 K (black, offset intensities). The calculated high spin Co(II) L-edge spectrum is represented in gray.

XAS line shape is typical for cyanide ligated Co(II) coordinated at the nitrogen end. Figure 5 compares the MP XAS with a ligand field multiplet calculation with parameters originally obtained from fitting to the XAS of $Co^{II}3[Cr^{III}(CN)_6]\cdot 12H_2O$.[10] Following adjustment of the total energy position such that the L-edges coincide, it is clear that the calculated spectral shape fits the CoFe MP spectrum accurately. Differences in the energy position relate to the effective nuclear charge on the Co metal ion, and thus the relative σ bonding to π back-bonding contribution. Despite this difference in comparison of the MP spectrum with the calculated ligand field multiplet spectrum, the coincidence of lines shapes confirms that Co(III) contributions to the MP are minimal.

The line shape of the DP Co L-edge spectrum differs from similarly ligated Co spectra reported for Prussian blue analogues of Fe(II)−CN−Co(III) connectivity,[18,19] as well as the single ion moiety, low spin Co(III) coordinated with nitrogen-end cyanide, $K_3Co^{III}(CN)_6$.[11] However, the six coordinate nitrogen cyanide atoms at the Co site in $K_3Co^{III}(CN)_6$ and Prussian blue analogues differ with respect CoFe where just two nitrogen cyanide atoms cis-coordinate, with the additional four sites coordinated to an (*R*)-pabn ligand. The similarity of the DP spectrum with respect to the MP spectrum make it difficult to infer the purity of the DP by XAS alone.

XMCD provides an atomic level probe of magnetism where XAS fails to provide sufficient resolution. Figure 6 shows the Co L-edge polarized μ^+ and μ^- Co absorption spectra measured at 15 K with a 1.9 T applied magnetic field. The MP becomes

dx.doi.org/10.1021/ic402580n | *Inorg. Chem.* 2013, 52, 13956−13962

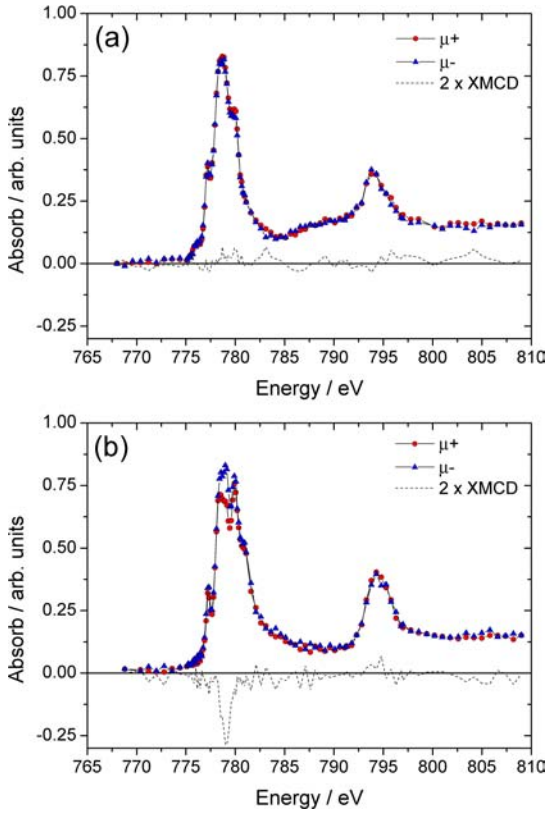

Figure 6. Polarized XAS and XMCD energy spectra for the Co L-edge of [CoFe] in the DP (a) and the MP (b) with an applied field of 1.9 T at 15 K.

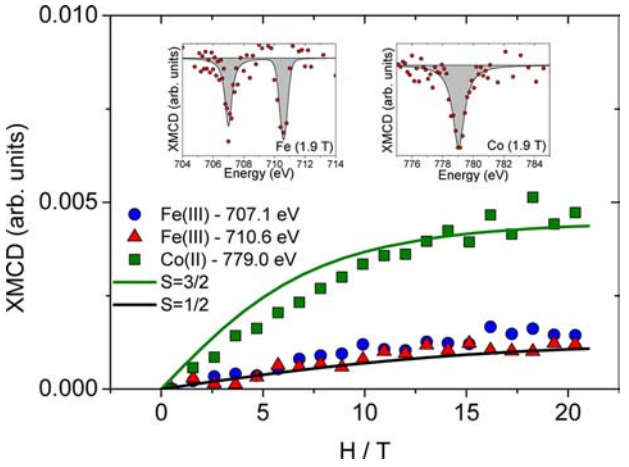

Figure 7. The XMCD magnetic field dependence measured at 10.7 K for [CoFe] in the magnetic phase for XAS energies exhibiting strong helicity dependence. The solid lines represent Brillouin function calculations for the $S = 3/2$ and $S = 1/2$ spin states for Co(II) and Fe(III). The two inserts show XMCD spectra for both the Fe and Co L_3-edges in the magnetic phase with an applied magnetic field of 1.9 T at 15 K, red circles. The back lines bounding the gray areas are fits of the three observed XMCD intensities.

strongly XMCD dependent unlike the DP, which exhibits a tiny helicity dependence associated with background noise. The lack of XMCD dependence in the DP Co and Fe L-edge spectra, in addition to the confirmation that the DP Fe L-edge XAS is consistent with pure LS Fe(II), suggests that the DP Co site contains at the very most, only a minor HS Co(II) contribution.

Pulsed Field XMCD. The MP XMCD for Co and Fe L_3-edge are compared by following their field dependence. The XMCD are surveyed up to 21 T over the L_3-edge for both the original DP and MP samples at 10.7 K to confirm the grinding assisted MMCT switching mechanism. The magnetic field dependence for the [CoFe] MP is shown in Figure 7, for the two Fe(III) XMCD intensity maxima (i and ii) and the center of the broad Co(II) XMCD intensity (779.0 eV). The magnetization curves follow typical Brillouin functions for paramagnetic behavior under a magnetic field, $S = 1/2$, $g = 2$ and $S = 3/2$, $g = 2.44$ for Fe and Co curves, respectively.

Grinding Assisted Switching Mechanism. The XMCD and XAS results characterize the grinding assisted Fe(II)Co(III) to Fe(III)Co(II) switching mechanism. Fe L-edge XAS and XMCD determine that the grinding assisted Co(LS-III)Fe(LS-II) to Co(HS-II)Fe(LS-III) MMCT is 75% efficient. The Co L-edge XAS shows a clear change in spectra on MMCT but the coincidence of the L-edge transitions for both phases make exact differentiation of the respective DP and MP contributions unquantifiable. However, XMCD measurements confirm that the DP CoFe does not exhibit paramagnetism, confirming the purity of the initial DM state to be Co(LS-III)Fe(LS-II). Magnetic susceptibility of a ground sample of [CoFe] also confirmed that it did not exhibit complete charge transfer, and a remnant thermal hysteresis on order of 10% of the total susceptibility is observed. Grinding was performed equivalently for both X-ray absorption and magnetic susceptibility cases, using the observed color change from green to dark red as an aid. Although it should be noted that the lack of precise quantification of the grinding process is a potential cause for discrepancy between the two measurement techniques. A second cause for the discrepancy in the grinding assisted MMCT could refer to the difference in measuring in the bulk (susceptibility) relative to the surface (XAS and XMCD).

The grinding assisted charge transfer process is similar to that observed in a chemically similar microporous cyanide-bridged chain, $[Fe(Tp)(CN)_3]_2Co(bpe)_5H_2O$, abbreviated $[Fe_2Co]$, where bpe =1,2-bis(4-pyridyl)ethane, which exhibits a dehydration induced MMCT switching, locking the system into a magnetic phase.[20] In the case of the $[Fe_2Co]$ cyanide-bridged chain, the origin of the switching process is associated with disturbance caused by the removal of three water molecules hydrogen bonded to terminal cyanide nitrogen atoms. This disturbance changes the redox at the Fe moiety destabilizing the Fe(II)Co(III) pairs in preference for the Fe(III)Co(II) phase. [CoFe] and $[Fe_2Co]$ share the same $Fe(Tp)(CN)_3$ ligand environment around the Fe metal ions. Within [CoFe], it has been reported that the loss of two water molecules results in a 20 K reduction of the thermally induced Fe(II)Co(III) to Fe(III)Co(II) MMCT transition temperature.[7] The effect of solvent alterations on the properties of [CoFe] and chemically related compounds highlights the sensitivity of the MMCT processes to small shifts in redox potential at metal ion moieties. Hence it is likely that the grinding assisted MMCT in [CoFe] is due to the final water molecule being forced out of the crystal, whereupon the redox potential at the LS Fe(II) is shifted to a negative potential resulting in the Fe(III)Co(II) magnetic phase being locked into place. The loss of the first two water molecules in [CoFe] could be inferred precisely by thermal gravimetric analysis. A fresh sample showed a weight decrease of 3.98% upon heating to 330 K; the ground sample

dx.doi.org/10.1021/ic402580n | Inorg. Chem. 2013, 52, 13956−13962

showed a weight loss of only 1.4% at the same temperature, confirming that the act of grinding had led to water loss.

Density Functional Theory Calculations. To support the XAS and XMCD measurements, calculations based on crystal structures measured at 100 and 295 K have been performed. An isotropic Heisenberg Hamiltonian, eq 1, is applied to characterize the magnetic exchange between Fe(III) and Co(II). The exchange constant (J) is estimated to be 10 cm^{-1}, determined by consideration of the calculated FM to AF energy gap and the $\langle S^2 \rangle$ values in accordance with Yamaguchi's formula,[21] eq 2.

$$\hat{H} = -2J\hat{s}_{Fe}\cdot\hat{s}_{Co} \quad (1)$$

$$J = \frac{E^{AF} - E^{F}}{\langle S^2\rangle^{F} - \langle S^2\rangle^{AF}} \quad (2)$$

Figure 8 compares selected DFT calculated eigenvalues of the [CoFe] molecular orbitals based on the 100 and 295 K

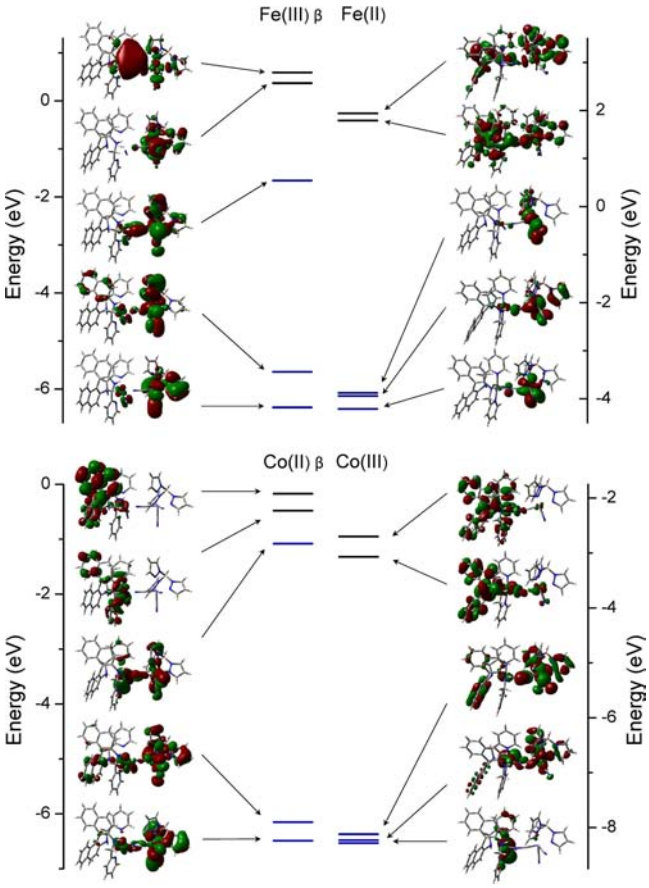

Figure 8. Comparison of Fe(II)Co(III) and FM Fe(III)Co(II) β magnetic orbitals calculated by DFT, based on 100 and 295 K crystal structures. The molecular orbitals demonstrate the degree of delocalization; red and green colors represent positive and negative signs of the wave function, respectively.

crystal structures. The spacial arrangement of the calculated orbital wave functions are overlaid on the structural unit as shown in Figure 2. Fe(II) and Co(III) of the DP are found to exhibit an energy configuration close to octahedral symmetry, giving average 10Dq energies of 5.88 and 5.3 eV respectively. The Fe(II) t_{2g} and Co(III) e_g are found to be strongly represented within the highest occupied molecular orbitals (HOMO to HOMO − 2) and lowest unoccupied molecular orbital (LUMO to LUMO + 1), respectively. However, the Fe(II) e_g and Co(III) t_{2g} contributing molecular orbitals are more difficult to identify due to delocalization through the surrounding ligand. It is assumed that the LUMO + 21 and LUMO + 23 are the Fe(II) e_g orbitals and the HOMO − 22 to HOMO − 24 are the Co(III) t_{2g} orbitals. Calculations of the Fe(III)Co(II) (295 K structure) FM phase β orbitals show a large shift away from the octahedral ligand field splitting determined for the diamagnetic Fe(II)Co(III) phase. Both Fe(III) and Co(II) exhibit energy splitting within the formally t_{2g} symmetry orbtials due to the combined effect of the MMCT process and related change in ligand field symmetry. The dramatic shift in orbital energy arrangement for Co(II) with respect to Co(III) evidence the spin crossover process. The 3d orbital wave functions for the FM Fe(III)Co(II) phase show extensive mixing with ligand orbitals. While it is possible to calculate the 2p orbital energies, effects such as core hole induced charge transfer, core hole−valence exchange, and multipole interactions make direct comparison of DFT calculated 2p to 3d orbital energies noncompatible with measured XAS.[22] The calculations here confirm how the change in temperature relates to a dramatic shift in electronic structure from Fe(II)Co(III) to Fe(III)Co(II) and the energetic preference for a ferromagnetic (FM) ground state within the 295 K structure. Finally calculation of the spin densities indicate low spin Fe and high spin Co for the 295 K structure, consistent with magnetometry and X-ray spectroscopy (see Supporting Information.

CONCLUSION

Measurements of L-edge XAS and XMCD up to high applied magnetic fields have been used to characterize a metal-to-metal charge transfer in a one-dimensional cyanide bridged [CoFe] chain. Diamagnetic low spin Fe(II) and Co(III) pairs within the chain compound are confirmed to exhibit an electron transfer and Co spin crossover, leading to magnetic low spin Fe(III) and high spin Co(II). XMCD is utilized to provide contrast between magnetic and nonmagnetic orbitals in the analysis of L-edge XAS. At the Fe(III) L_3-edge, XMCD aids the identification of cyanide π^* orbital back-bonding state exhibiting wave function hybridization with the unpaired electron carrying Fe(III) orbital, highlighting the MMCT pathway. XMCD at the Co L-edge discriminates the Co site valence compositions, where differentiation via XAS spectral features is limited. An additional switching mechanism is determined for [CoFe] adding grinding assisted (dehydration) MMCT to the previously characterized photon illumination and heat induced MMCT processes. XAS and XMCD characterize the grinding induced charge transfer to be 75% efficient. DFT calculations based on the DP and the MP crystal structures, 100 and 295 K, respectively, calculate the energy and orbital delocalization of the molecular orbitals, uncovering the changes in the 3d orbital energies following the electron transfer process. The DFT calculations are consistent with the spectroscopically obtained results.

ASSOCIATED CONTENT

Supporting Information

A complete collection of DFT results including calculated molecular orbitals and energies for the diamagnetic phase and magnetic, antiferromagnetic, and ferromagnetic cases for α and

dx.doi.org/10.1021/ic402580n | Inorg. Chem. 2013, 52, 13956−13962

β electron configurations. This material is available free of charge via the Internet at http://pubs.acs.org.

AUTHOR INFORMATION

Corresponding Author

*E-mail: nojiri@imr.tohoku.ac.jp.

Notes

The authors declare no competing financial interest.

ACKNOWLEDGMENTS

The synchrotron radiation experiments were performed at the BL25SU of SPring-8 with the approval of the Japan Synchrotron Radiation Research Institute (JASRI) (Proposal No. 2011B1242, 2012A1430, and 2012B1557). M. L. Baker thanks the Japanese Society for the Promotion of Science for a postdoctoral fellowship. Grant-in-Aid for Scientific Research on Innovative Areas "Coordination programming" from the Ministry of Education, Culture, Sports, Science and Technology (MEXT) is also acknowledged.

REFERENCES

(1) (a) Gaspar, A. B.; Ksenofontov, V.; Seredyuk, M.; Gütlich, P. *Coord. Chem. Rev.* **2005**, *249*, 2661−2676. (b) Shimamoto, N.; Ohkoshi, S.-i.; Sato, O.; Hashimoto, K. *Inorg. Chem.* **2002**, *41*, 678−684.

(2) (a) Sato, O.; Tao, J.; Zhang, Y.-Z. *Angew. Chem., Int. Ed.* **2007**, *46*, 2152−2187. (b) Bousseksou, A.; Molnar, G.; Salmon, L.; Nicolazzi, W. *Chem. Soc. Rev.* **2011**, *40*, 3313−3335. (c) Bleuzen, A.; Marvaud, V.; Mathoniere, C.; Sieklucka, B.; Verdaguer, M. *Inorg. Chem.* **2009**, *48*, 3453−3466. (d) Cafun, J.-D.; Lejeune, J.; Itié, J.-P.; Baudelet, F.; Bleuzen, A. *J. Phys. Chem. C* **2013**, *117*, 19645−19655.

(3) (a) Ferlay, S.; Mallah, T.; Ouahes, R.; Veillet, P.; Verdaguer, M. *Nature* **1995**, *378*, 701. (b) Sato, O.; Iyoda, T.; Fujishima, A.; Hashimoto, K. *Science* **1996**, *272*, 704−705. (c) Herrera, J.; Bachschmidt, A.; Villain, F.; Bleuzen, A.; Marvaud, V.; Wernsdorfer, W.; Verdaguer, M. *Philos. Trans. R. Soc., A* **2008**, *366*, 127−138.

(4) (a) Newton, G. N.; Nihei, M.; Oshio, H. *Eur. J. Inorg. Chem.* **2011**, *2011*, 3031−3042. (b) Nihei, M.; Sekine, Y.; Suganami, N.; Nakazawa, K.; Nakao, A.; Nakao, H.; Murakami, Y.; Oshio, H. *J. Am. Chem. Soc.* **2011**, *133*, 3592−3600. (c) Oshio, H.; Onodera, H.; Tamada, O.; Mizutani, H.; Hikichi, T.; Ito, T. *Chem.—Eur. J.* **2000**, *6*, 2523−2530. (d) Mondal, A.; Li, Y.; Seuleiman, M.; Julve, M.; Toupet, L.; Buron-Le Cointe, M.; Lescouëzec, R. *J. Am. Chem. Soc.* **2013**, *135*, 1653−1656.

(5) (a) Liu, T.; Zhang, Y.-J.; Kanegawa, S.; Sato, O. *J. Am. Chem. Soc.* **2010**, *132*, 8250−8251. (b) Ouellette, W.; Prosvirin, A.; Whitenack, K.; Dunbar, K.; Zubieta, J. *Angew. Chem., Int. Ed.* **2009**, *48*, 2140−2143. (c) Hoshino, N.; Sekine, Y.; Nihei, M.; Oshio, H. *Chem. Commun.* **2010**, *46*, 6117−6119. (d) Yoon, J. H.; Ryu, D. W.; Choi, S. Y.; Kim, H. C.; Koh, E. K.; Tao, J.; Hong, C. S. *Chem. Commun.* **2011**, *47*, 10416−10418.

(6) Miyasaka, H.; Julve, M.; Yamashita, M.; Clérac, R. *Inorg. Chem.* **2009**, *48*, 3420−3437.

(7) Hoshino, N.; Iijima, F.; Newton, G. N.; Norifumi, Y.; Takuya, S.; Akiko, N.; Youichi, M.; Hiroyuki, N.; Oshio, H. *Nat. Chem.* **2012**, *4*, 921−926.

(8) (a) de Groot, F. *Coord. Chem. Rev.* **2005**, *249*, 31−63. (b) Stöhr, J. *J. Magn. Magn. Mater.* **1999**, *200*, 470−497.

(9) Hocking, R. K.; Wasinger, E. C.; de Groot, F. M. F.; Hodgson, K. O.; Hedman, B.; Solomon, E. I. *J. Am. Chem. Soc.* **2006**, *128*, 10442−10451.

(10) Arrio, M.-A.; Sainctavit, P.; Cartier dit Moulin, C.; Mallah, T.; Verdaguer, M.; Pellegrin, E.; Chen, C. T. *J. Am. Chem. Soc.* **1996**, *118*, 6422−6427.

(11) Cartier dit Moulin, C.; Villain, F.; Bleuzen, A.; Arrio, M.-A.; Sainctavit, P.; Lomenech, C.; Escax, V.; Baudelet, F.; Dartyge, E.; Gallet, J.-J.; Verdaguer, M. *J. Am. Chem. Soc.* **2000**, *122*, 6653−6658.

(12) Coronado, E.; Giménez-López, M. C.; Korzeniak, T.; Levchenko, G.; Romero, F. M.; Segura, A.; García-Baonza, V.; Cezar, J. C.; de Groot, F. M. F.; Milner, A.; Paz-Pasternak, M. *J. Am. Chem. Soc.* **2008**, *130*, 15519−15532.

(13) Hocking, R. K.; Wasinger, E. C.; Yan, Y.-L.; deGroot, F. M. F.; Walker, F. A.; Hodgson, K. O.; Hedman, B.; Solomon, E. I. *J. Am. Chem. Soc.* **2007**, *129*, 113−125.

(14) Cornia, A.; Mannini, M.; Sainctavit, P.; Sessoli, R. *Chem. Soc. Rev.* **2011**, *40*, 3076−3091.

(15) (a) Kuepper, K.; Derks, C.; Taubitz, C.; Prinz, M.; Joly, L.; Kappler, J.-P.; Postnikov, A.; Yang, W.; Kuznetsova, T. V.; Wiedwald, U.; Ziemann, P.; Neumann, M. *Dalton Trans.* **2013**, *42*, 7924−7935. (b) Ghigna, P.; Campana, A.; Lascialfari, A.; Caneschi, A.; Gatteschi, D.; Tagliaferri, A.; Borgatti, F. *Phys. Rev. B* **2001**, *64*, No. 132413. (c) Lorusso, G.; Corradini, V.; Ghirri, A.; Biagi, R.; del Pennino, U.; Siloi, I.; Troiani, F.; Timco, G.; Winpenny, R. E. P.; Affronte, M. *Phys. Rev. B* **2012**, *86*, No. 184424.

(16) Mannini, M.; Pineider, F.; Sainctavit, P.; Danieli, C.; Otero, E.; Sciancalepore, C.; Talarico, A. M.; Arrio, M.-A.; Cornia, A.; Gatteschi, D.; Sessoli, R. *Nat. Mater.* **2009**, *8*, 194.

(17) Nakamura, T.; Narumi, Y.; Hirono, T.; Hayashi, M.; Kodama, K.; Tsunoda, M.; Isogami, S.; Takahashi, H.; Kinoshita, T.; Kindo, K.; Nojiri, H. *Appl. Phys. Express* **2011**, *4*, 066602.

(18) Bonhommeau, S.; Pontius, N.; Cobo, S.; Salmon, L.; de Groot, F. M. F.; Molnar, G.; Bousseksou, A.; Durr, H. A.; Eberhardt, W. *Phys. Chem. Chem. Phys.* **2008**, *10*, 5882−5889.

(19) Cafun, J.-D.; Champion, G.; Arrio, M.-A.; dit Moulin, C. C.; Bleuzen, A. *J. Am. Chem. Soc.* **2010**, *132*, 11552−11559.

(20) Liu, T.; Zhang, Y.-J.; Kanegawa, S.; Sato, O. *Angew. Chem., Int. Ed.* **2010**, *49*, 8645−8648.

(21) Soda, T.; Kitagawa, Y.; Onishi, T.; Takano, Y.; Shigeta, Y.; Nagao, H.; Yoshioka, Y.; Yamaguchi, K. *Chem. Phys. Lett.* **2000**, *319*, 223−230.

(22) Stavitski, E.; de Groot, F. M. *Micron* **2010**, *41*, 687−694.